










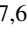







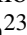



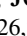
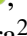










The metamorphosis of the Type Ib SN 2019yvr: late-time interaction

Lucía Ferrari,^{1,2} * Gastón Folatelli,^{1,2,3} , Hanindyo Kuncarayakti^{4,5} , Maximilian Stritzinger⁶ , Keiichi Maeda⁷ , Melina Bersten^{1,2,3}, Lili M. Román Aguilar^{1,2} , M. Manuela Sáez^{8,9} , Luc Dessart¹⁰ , Peter Lundqvist¹¹, Paolo Mazzali^{12,13} , Takashi Nagao^{4,14,15} , Chris Ashall¹⁶ , Subhash Bose^{17,6} , S. J. Brennan¹¹ , Y.-Z. Cai^{18,19,20} , Rasmus Handberg⁶ , Simon Holmbo⁶ , Emir Karamehmetoglu⁶ , Andrea Pastorello²¹ , Andrea Reguitti^{21,22} , Joseph Anderson²³ , Ting-Wan Chen²⁴ , Lluís Galbany^{25,26} , Mariusz Gromadzki²⁷ , Claudia P. Gutiérrez^{26,25} , Cosimo Inserra²⁸ , Erkki Kankare⁴ , Tomás E. Müller Bravo^{25,26} , Seppo Mattila^{4,29} , Matt Nicholl³⁰ , Giuliano Pignata³¹ , Jesper Sollerman¹¹ , Shubham Srivastav³² , David R. Young³² 

¹Instituto de Astrofísica de La Plata, CONICET, Argentina

²Facultad de Ciencias Astronómicas y Geofísicas Universidad Nacional de La Plata, Paseo del Bosque S/N B1900FWA, La Plata, Argentina

³Kavli Institute for the Physics and Mathematics of the Universe (WPI), The University of Tokyo, Kashiwa, 277-8583 Chiba, Japan

⁴Department of Physics and Astronomy, University of Turku, FI-20014 Turku, Finland

⁵Finnish Centre for Astronomy with ESO (FINCA), FI-20014 University of Turku, Finland

⁶Department of Physics and Astronomy, Aarhus University, Ny Munkegade 120, DK-8000 Aarhus C, Denmark

⁷Department of Astronomy, Kyoto University, Kitashirakawa-Oiwake-cho, Sakyo-ku, Kyoto, 606-8502, Japan

⁸Interdisciplinary Theoretical and Mathematical Sciences Program (iTHEMS), RIKEN, Wako, Saitama 351-0198, Japan

⁹Department of Physics, University of California, Berkeley, CA 94720

¹⁰Institut d'Astrophysique de Paris, CNRS-Sorbonne Université, 98 bis boulevard Arago, 75014 Paris, France

¹¹The Oskar Klein Centre, Department of Astronomy, Stockholm University, AlbaNova, SE-10691 Stockholm, Sweden

¹²Max-Planck-Institut für Astrophysik, Karl-Schwarzschild-Str. 1, D-85748 Garching, Germany

¹³Astrophysics Research Institute, Liverpool John Moores University, 146 Brownlow Hill, Liverpool L3 5RF, UK

¹⁴Aalto University Metsähovi Radio Observatory, Metsähovintie 114, 02540 Kylmälä, Finland

¹⁵Aalto University Department of Electronics and Nanoengineering, P.O. BOX 15500, FI-00076 AALTO, Finland

¹⁶Department of Physics, Virginia Tech, Blacksburg, VA 24061, USA

¹⁷Department of Astronomy, The Ohio State University, 140 W. 18th Avenue, Columbus, OH 43210, USA

¹⁸Yunnan Observatories, Chinese Academy of Sciences, Kunming 650216, P.R. China

¹⁹Key Laboratory for the Structure and Evolution of Celestial Objects, Chinese Academy of Sciences, Kunming 650216, P.R. China

²⁰International Centre of Supernovae, Yunnan Key Laboratory, Kunming 650216, P.R. China

²¹INAF - Osservatorio Astronomico di Padova, Vicolo dell'Osservatorio 5, 35122 Padova, Italy

²²INAF - Osservatorio Astronomico di Brera, Via E. Bianchi 46, 23807 Merate (LC), Italy

²³European Southern Observatory, Alonso de Córdova 3107, Casilla 19, Santiago, Chile

²⁴Graduate Institute of Astronomy, National Central University, 300 Jhongda Road, 32001 Jhongli, Taiwan

²⁵Institute of Space Sciences (ICE-CSIC), Campus UAB, Carrer de Can Magrans, s/n, E-08193 Barcelona, Spain

²⁶Institut d'Estudis Espacials de Catalunya (IEEC), E-08034 Barcelona, Spain

²⁷Astronomical Observatory, University of Warsaw, Al. Ujazdowskie 4, 00-478 Warszawa, Poland

²⁸School of Physics and Astronomy, Cardiff University, Queens Buildings, The Parade, Cardiff CF24 3AA, UK

²⁹School of Sciences, European University Cyprus, Diogenes Street, Engomi, 1516, Nicosia, Cyprus

³⁰Astrophysics Research Centre, School of Mathematics and Physics, Queens University Belfast, Belfast BT7 1NN, UK

³¹Instituto de Alta Investigación, Universidad de Tarapacá, Casilla 7D, Arica, Chile

³²Astrophysics Research Centre, School of Mathematics and Physics, Queen's University Belfast, BT7 1NN, UK

Accepted XXX. Received YYY; in original form ZZZ

ABSTRACT

We present observational evidence of late-time interaction between the ejecta of the hydrogen-poor Type Ib supernova (SN) 2019yvr and hydrogen-rich circumstellar material (CSM), similar to the Type Ib SN 2014C. A narrow H α emission line appears simultaneously with a break in the light-curve decline rate at around 80 – 100 d after explosion. From the interaction delay and the ejecta velocity, under the assumption that the CSM is detached from the progenitor, we estimate the CSM inner radius to be located at $\sim 6.5 - 9.1 \times 10^{15}$ cm. The H α emission line persists throughout the nebular phase at least up to +420 d post-explosion, with a full width at half maximum (FWHM) of ~ 2000 km s⁻¹. Assuming a steady mass loss, the estimated mass-loss rate from the luminosity of the H α line is $\sim 3 - 7 \times 10^{-5} M_{\odot} \text{ yr}^{-1}$. From hydrodynamical modeling and analysis of the nebular spectra, we find a progenitor He-core mass of $3 - 4 M_{\odot}$, which would imply an initial mass of $13 - 15 M_{\odot}$. Our result supports the case of a relatively low mass progenitor possibly in a binary system as opposed to a higher mass single star undergoing an LBV phase.

Key words: supernovae: general – supernovae: individual: SN 2019yvr –

1 INTRODUCTION

Supernovae (SNe) are among the most powerful explosions in the Universe, and their study provides valuable insights into a multitude of astrophysical processes including stellar evolution, the subsequent formation of compact objects, and the chemical enrichment of the Universe. A substantial fraction of SNe are associated with the collapse of the iron cores of massive stars, called core-collapse SNe (CCSNe). CCSNe are classified based on their spectral characteristics. Objects with H features are classified as Type II, those lacking H but exhibiting He are of Type Ib, and those with no H nor He are of Type Ic (for a contemporary and concise review, see [Stritzinger et al. 2023b](#), and references therein). Although relatively rare, the H-poor stripped-envelope (SE) SNe are of particular interest as they are most likely linked to the death of a He or C+O star, as an analog of Wolf-Rayet stars, which experienced significant mass loss either through strong stellar winds or interaction with a binary companion (e.g., [Woosley et al. 1993](#); [Podsiadlowski et al. 2004](#); [Smith 2014](#)). Moreover, it has been proposed that the progenitor envelope could be removed by a combination of both processes, i. e. hybrid mass-loss ([Fang et al. 2019](#); [Sun et al. 2023](#)).

A small but growing number of Type Ib (e.g., [Milisavljevic et al. 2015](#); [Vinko et al. 2017](#); [Mauerhan et al. 2018](#); [Chandra et al. 2020](#)) and Type Ic SNe ([Kuncarayakti et al. 2018](#); [Tartaglia et al. 2021](#); [Stritzinger et al. 2023a](#)) exhibit signatures of circumstellar interaction (CSI) in optical wavelengths. CSI occurs when rapidly expanding SN ejecta shock a dense circumstellar material (CSM), originated from the progenitor star itself, or from a companion star (e.g., [Chevalier & Fransson 1994](#); [Fransson et al. 2002](#); [Yoon 2017](#)). Signatures of CSI in some cases are revealed in the spectra as narrow Balmer emission lines, reminiscent to the hallmark feature of Type II_n SNe (e.g., [Schlegel 1990](#); [Taddia et al. 2013](#)), as well as in some cases high-ionization coronal lines, and/or excesses of flux in different regions of the electromagnetic spectrum (e.g., [Stritzinger et al. 2012](#)).

In this paper we examine SN 2019yvr, which was initially classified as a Type Ib SN ([Dimitriadis 2019](#)), but eventually developed SN II_n-like features. Based on pre-explosion Hubble Space Telescope (HST) archival images, [Kilpatrick et al. \(2021\)](#) found a point source at the location of SN 2019yvr. The spectral energy distribution (SED) of the source suggests a cool and luminous progenitor candidate, in contradiction with the He star picture of a SN Ib progenitor. They also discuss a binary scenario but also find it incompatible with a Type Ib SN progenitor. [Sun et al. \(2022\)](#) explored several scenarios by performing an environmental study, and proposed a binary system, composed of a hot and compact SN progenitor and a yellow hypergiant (YHG) companion. SN 2019yvr therefore provides an opportunity to understand better the pre-SN evolution of interacting events' progenitors.

The present work focuses on the appearance of the CSI features in SN 2019yvr, the late-time interaction, and particular progenitor properties such as the pre-SN mass and mass-loss rate. We will complement this analysis with an upcoming paper by Ferrari et al. (in prep.) where we will provide a detailed analysis of the full photometric and spectroscopic evolution.

2 OBSERVATIONS

SN 2019yvr was first reported by the Asteroid Terrestrial-impact Last Alert System (ATLAS) on 2019 December 27.5 UT ([Tonry et al. 2019](#)), and classified two days later as a Type Ib SN ([Dimitriadis et al. 2019](#); [Muller et al. 2019](#)). Based on the last non-detection

from the Zwicky Transient Facility (ZTF, [Masci et al. 2019](#)), we adopt an explosion epoch as $JD = 2458839.89 \pm 3.84$. The SN is located in the nearby Galaxy NGC 4666, which hosted the Type Ia SN ASASSN-14lp ([Shappee et al. 2016](#)). We adopt their derived distance of 14.7 ± 1.5 Mpc. See Sec. 1 of the Supplementary Material for details on the discovery, the estimated explosion date and the adopted distance.

The data employed in this study are part of a larger set of multiband optical light curves and a series of spectra (Ferrari et al., in prep.). Here we present *BVgri*-band photometry measured from images obtained by the NUTS¹ (Nordic optical telescope Un-biased Transient Survey) and ASAS-SN² (All-Sky Automated Survey for Supernovae) collaborations using the 2.56-m NOT telescope equipped with ALFOOSC (Andalucia Faint Object Spectrograph and Camera) and the 1-m Las Cumbres Observatory Global Telescope (LCOGT) network respectively. The NOT images were reduced using the *pyraf*-based ALFOOSCGUI³ reduction pipeline developed by E. Cappellaro, while fully processed LCOGT images were downloaded from the observatory's data archive.

Host-galaxy subtraction was performed on all science frames using template images obtained prior to 2019. Point-spread-function (PSF) photometry of SN 2019yvr was then measured relative to stars in the field using the Aarhus-Barcelona FLOWS project's automated pipeline⁴. The photometry is tabulated in Sec. 2 of the Supplementary Material.

We also present eight low-resolution and one high-resolution optical spectra, which are summarized in the journal of spectroscopic observations (Sec. 2 of the Supplementary Material). In summary, four spectra were obtained by ePESSTO+ ([Smartt et al. 2015](#)) with the European Southern Observatory (ESO) 3.58-m New Technology Telescope (NTT, [Buzzoni et al. 1984](#)) equipped with the ESO Faint Object Spectrograph and Camera optical (EFOSC2), three by NUTS with the NOT (+ ALFOOSC), and one spectrum was obtained with the ESO 8.4-m Very Large Telescope (VLT) FOcal Reducer and low dispersion Spectrograph (FOR2, [Appenzeller et al. 1998](#)), as part of the FORS+ Survey of Supernovae in Late Times program (FOSSIL; see [Kuncarayakti et al. 2022](#)). A high-resolution spectrum was obtained with the 8.2-m Subaru Telescope equipped with the High Dispersion Spectrograph (HDS, [Noguchi et al. 2002](#)). The spectroscopic observations were reduced following standard techniques using the respective instrument pipelines.

The Milky Way reddening along the line-of-sight is $E(B-V)_{MW} = 0.022$ mag (i.e., $A_V^{MW} = 0.068$ mag, [Schlafly & Finkbeiner 2011](#), assuming $R_V = 3.1$). After comparing the observed color curves of SN 2019yvr with the intrinsic color-curve templates from [Stritzinger et al. 2018](#), analyzing the diffuse interstellar band (DIB) at 5780 Å and the Na I D lines in the high-resolution spectrum from the Subaru telescope, we adopt a host-galaxy reddening of $E(B-V)_{host} = 0.57 \pm 0.09$ mag. This value is in agreement with the estimate of [Kilpatrick et al. \(2021\)](#) of $0.51^{+0.27}_{-0.16}$ mag and with that published in [Rodríguez et al. \(2022\)](#) of 0.56 ± 0.09 mag. Details on the reddening estimation are presented in Sec. 3 of the Supplementary Material.

¹ <http://nuts.sn.ie/>

² <https://www.astronomy.ohio-state.edu/asassn/>

³ <http://graspa.oapd.inaf.it/foscgui.html>

⁴ <https://github.com/SNflows>

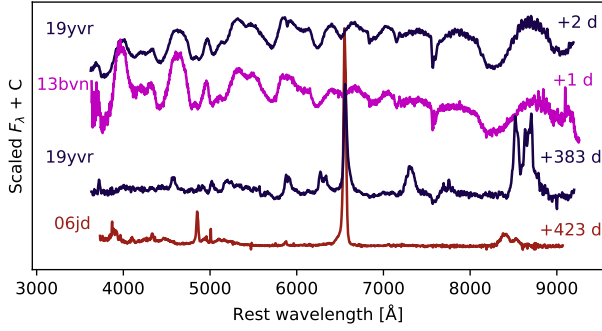


Figure 1. SN 2019yvr transitions from a SN Ib spectrum around maximum to a Type IIn-like spectrum at late phase. Comparison data include a similar phase spectrum of the SN Ib iPTF13bvn (Srivastav et al. 2014) and the Type IIn SN 2006jd (Stritzinger et al. 2012). Spectra are corrected by redshift and not corrected by extinction.

3 SIGNATURES OF CSM INTERACTION

3.1 Emergence of $H\alpha$ emission

SN 2019yvr showed $H\alpha$ emission at late times similarly to SN 2014C, which in that case was interpreted as a result of interaction between the ejecta and H-rich CSM (e.g. Milisavljevic et al. 2015; Margutti et al. 2017). In Fig. 1 we compare the spectra of SN 2019yvr obtained +2 days (d) and +383 d past the epoch of B -band maximum, JD= 2458851.6 (see Table 1 of the Supplementary Material). Throughout the paper we will refer the phases to this date unless otherwise specified. While the first spectrum is consistent with that of typical SNe Ib, the late-phase spectrum clearly exhibits the transformation to a SN IIn-like spectrum.

The temporal coverage of SN 2019yvr observations allows us to study the moment when signatures of interaction become apparent. This is depicted in Fig. 2 where we show the evolution of the spectra around the $\text{He I } \lambda 6678$ (which includes $H\alpha$) and the $\text{He I } \lambda 7065$ lines between +42 d and +118 d. The +118 d spectrum clearly exhibits $H\alpha$ in emission, whereas the previous spectra show an absorption at the same wavelength. While the absorption due to $\text{He I } \lambda 6678$ becomes substantially weaker with time before the $H\alpha$ emission emerges, the absorption due to $\text{He I } \lambda 7065$ remains roughly constant.

This phenomenon can be appreciated in the evolution of the absorption pseudo-equivalent width (pEW)⁵ of both lines. We measured pEW using the *splot* task from IRAF five times to account for values with their corresponding errors. For $\text{He I } \lambda 6678$ we obtain $\text{pEW} = 40.4 \pm 0.9, 26.9 \pm 0.6, \text{ and } 10.4 \pm 0.3 \text{ \AA}$ at 42, 59, and 79 d, respectively, whereas for $\text{He I } \lambda 7065$ the values are nearly constant or even rising ($91 \pm 1.4, 106 \pm 1.4, \text{ and } 118 \pm 2.2 \text{ \AA}$). The same behavior as that of $\text{He I } \lambda 7065$ is seen in $\text{He I } \lambda 5876$ but we note that the Na I D doublet may contaminate the latter line and thus it is not shown here. We interpret the weakening of the $\text{He I } \lambda 6678$ absorptions as a result of the appearance of $H\alpha$ in emission at a similar wavelength.

Assuming a detached CSM from the progenitor, we conclude that the strong ejecta–CSM interaction initiated sometime prior to +79 d.

⁵ The term ‘pseudo-equivalent width’ is used because the actual continuum flux is unknown and we therefore fit a ‘pseudo-continuum’ between the local maxima at both sides of the line.

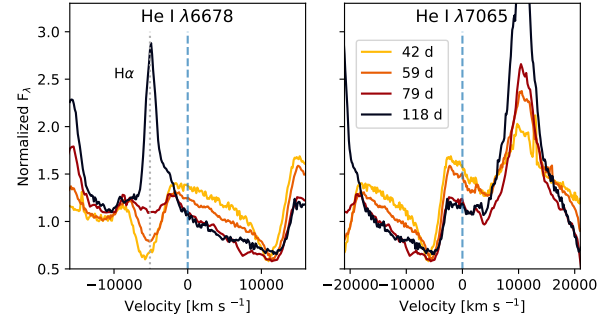


Figure 2. Evolution of the $\text{He I } \lambda 6678$ and $\text{He I } \lambda 7065$ features of SN 2019yvr from +42 d to +118 d plotted in velocity space. Dashed vertical lines indicate the 0 km s^{-1} position, while in the left panel the dotted vertical line indicates the rest wavelength of $H\alpha$. Complete spectra are displayed in Sec. 4 of the Supplementary Material.

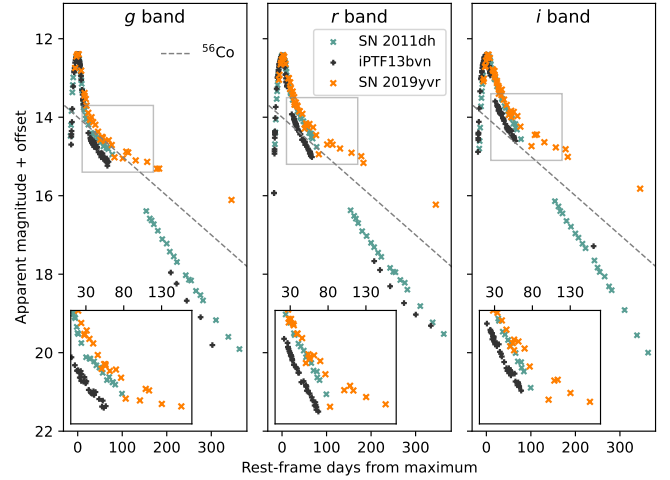


Figure 3. Light curves of SN 2019yvr compared with those of SN 2011dh (Ergon et al. 2015) and iPTF13bvn (Fremling et al. 2016), shifted in magnitudes to coincide at the peak. Gray dashed lines correspond to ^{56}Co decay. The post-maximum light curves of SN 2019yvr begin to deviate from the normal decay line of the comparison objects beginning around +80 d.

3.2 Flattening in the light curves

The *gri*-band light curves are plotted in Fig. 3, compared with the Type IIn SN 2011dh and the Type Ib iPTF13bvn. The light curves of SN 2019yvr present a characteristic break in the post-maximum decline rate, leading to a flattening after +90 d. In Fig. 3 the break is evident in all optical bands by comparison with supernovae that show a similar evolution around maximum light. Moreover, iPTF13bvn provided a very good match to the spectroscopic evolution of SN 2019yvr around maximum light. Although the spectral match to the SN IIn 2011dh is worse, its light curves provide a good match to our object around maximum light and are more complete than those of iPTF13bvn.

We interpret the sudden change in the slope of the light curves of SN 2019yvr as a result of an extra power source caused by sustained interaction between the SN ejecta and the CSM. This interpretation is supported by the nearly simultaneous appearance of $H\alpha$ emission in the spectra (see Section 3.1). From close inspection of Fig. 3, we conclude that the flattening in the light curves occurs in all bands

between +70 and +90 d with respect to maximum light. This is in accordance with what was found in Section 3.1.

3.3 Properties of the CSM

Based on the light curves and spectral evolution, we have determined that the interaction power starts dominating the decay power between +70 d to +90 d (i.e., 75 – 105 d post our inferred explosion epoch). If we assume the presence of a detached CSM structure, the interaction delay indicates a distance to its inner boundary. By adopting a maximum ejecta velocity of $\sim 10,000 \text{ km s}^{-1}$ from the bluest extent of the He I $\lambda\lambda 6678, 7065$ absorption components, this gives a distance of $6.5 - 9.1 \times 10^{15} \text{ cm}$ or $0.9 - 1.3 \times 10^5 R_{\odot}$. These values are comparable to those obtained for SN 2001em (a SN Ic that showed late phase H α in emission, Chugai & Chevalier 2006); and SN 2014C (Milisavljevic et al. 2015). If the CSM was expelled by stellar winds with a velocity in the range of $50 - 100 \text{ km s}^{-1}$, the mass loss must have occurred up until $\sim 20 - 60$ years prior to the explosion (assuming a detached CSM).

We further study the properties of the CSM by analyzing the H α emission in the nebular phase. We measure the H α luminosity, $L_{H\alpha}$, to derive the mass-loss rate from (e.g. Kuncarayakti et al. 2018)

$$\dot{M} = 2 \frac{L_{H\alpha}}{\epsilon_{H\alpha}} \frac{v_{\text{wind}}}{v_{\text{shock}}^3},$$

where v_{wind} is the wind velocity at which the material was expelled during the final stages of the star's evolution, v_{shock} is the velocity of the colliding material, and $\epsilon_{H\alpha}$ is an efficiency factor that we assume to be 0.01 (Chevalier & Fransson 1994).

We scaled our +383 d and +386 d spectra so that they matched the r -band photometry. They were corrected for extinction and the H α fluxes were then measured with `splot` in IRAF. We discard the measurement from the +426d spectrum because it likely suffers from host-galaxy contamination. The resulting fluxes were $7.77 \pm 0.19 \times 10^{-14} \text{ erg s}^{-1} \text{ cm}^{-2}$ from the +383 d spectrum, and $8.44 \pm 0.44 \times 10^{-14} \text{ erg s}^{-1} \text{ cm}^{-2}$ from the +386 d spectrum, whose average yields a flux of $8.10 \pm 0.47 \times 10^{-14} \text{ erg s}^{-1} \text{ cm}^{-2}$. With the distance given in Section 2, we obtained an H α luminosity of $L_{\alpha} = 2.1 \pm 0.6 \times 10^{39} \text{ erg s}^{-1}$. For the shock velocity, we adopted $10,000 \text{ km s}^{-1}$ based on typical values for SNe Ib (Liu et al. 2016). Assuming a wind velocity of $v_{\text{wind}} = 50 - 100 \text{ km s}^{-1}$, the derived mass-loss rate range is $\sim 3 - 7 \times 10^{-5} M_{\odot} \text{ yr}^{-1}$. This is comparable to that of SN 2013df, which also shows a late-phase light curve flattening (Maeda et al. 2015). If a shock velocity of $2,000 \text{ km s}^{-1}$ is considered, this translates to an upper limit for the mass-loss rate of $\sim 4 - 8 \times 10^{-3} M_{\odot} \text{ yr}^{-1}$. A high density of the CSM may prevent the appearance of [O III] lines, but would not be enough to produce electron scattering wings in H α (see Sec. 4). The material could be distributed in a clumpy shell with cloud shocks of about $2,000 \text{ km s}^{-1}$ and faster, lower-density shocks in between, which would be responsible for the H α wings.

4 NEBULAR SPECTRA

Nebular spectra of SN 2019yvr obtained on +383 d, +386 d and +426 d are plotted in Fig. 4, along with a +371 d spectrum of SN 2014C and a +290 d spectrum of iPTF13bvn. These objects were classified as H-poor SNe Ib based on their early spectroscopy⁶. Sim-

⁶ Note that some authors suggested the possible presence of H features in the spectra of iPTF13bvn and SN 2014C (Kuncarayakti et al. 2015; Milisavljevic et al. 2015).

ilar to SN 2014C, SN 2019yvr developed a narrow $\sim 2000 \text{ km s}^{-1}$ H α emission at late times, although their profiles differ. While in SN 2019yvr the line is asymmetric and blue-shifted by $\sim 300 \text{ km s}^{-1}$, SN 2014C showed a compound profile, with one broad $\sim 1200 \text{ km s}^{-1}$ component overlapped with narrow $\sim 250 \text{ km s}^{-1}$ H α and [N II] $\lambda\lambda 6548, 6583$ components (Milisavljevic et al. 2015). The narrow components may be linked to CSM material undergoing photoionization caused by X-rays emitted by the interaction, though these could also result from contamination by an underlying H II region. The broad component is associated with the shock or ejected material colliding with the CSM. In the right panel of Fig. 4 we rebinned the spectrum of SN 2014C to match the resolution of the FORS spectrum of SN 2019yvr. We conclude that those narrow lines, if present, are not resolved by our observations. Another difference can be appreciated in the narrow emissions associated with H β and [O III] $\lambda\lambda 4959, 5007$ that are absent in the case of SN 2019yvr.

A striking feature is the strong Ca II near-infrared triplet, which is usually weaker than [O I] $\lambda\lambda 6300, 6364$ and [Ca II] $\lambda\lambda 7291, 7324$ in SESNe (Jerkstrand et al. 2015; Dessart et al. 2021, 2023a). This feature is detected in the +282 d spectrum of SN 2014C, but with a substantially weaker intensity (Milisavljevic et al. 2015) compared to SN 2019yvr.

Typical nebular emission lines are present, such as the aforementioned [O I], [Ca II], also Na I D, and Mg I $\lambda 4571$. The oxygen doublet shows a double-peaked profile, with a $\sim 1300 \text{ km s}^{-1}$ blueshift and a FWHM of ~ 2000 and $\sim 2500 \text{ km s}^{-1}$ for the bluer and redder component respectively, different from the one-component profile in SN 2014C. The Na I D emission presents a broad profile, with ISM absorption on top. The [Ca II] and Mg I lines show a single component profile. Line identifications are shown in Fig. 4.

The H α profile provides insights into the geometry responsible for such emission. If the CSM was distributed in a spherical structure surrounding the SN, the profile should be box-shaped as in SN 1993J (Filippenko et al. 1994; Patat et al. 1995; Matheson et al. 2000) and SN 2013df (Maeda et al. 2015). The absence of such a profile suggests that the emission may not come from the outer layers of the ejecta interacting with the CSM, as the velocity should be higher ($\sim 10000 \text{ km s}^{-1}$, see e.g. Dessart et al. 2023b). The $\sim 2000 \text{ km s}^{-1}$ width of the H α line indicates that the slower, inner part of the ejecta are interacting with a nearby, dense CSM. This CSM may take the form of a circumstellar disk which could be produced in a binary system, although detailed modeling is required to ascertain this possibility. It has been proposed for SN 2014C that the H α emission comes from the interaction between the ejecta and a CSM with a torus-like structure (Thomas et al. 2022), which could be also the case for SN 2019yvr.

5 PROGENITOR PROPERTIES

In this section, we aim to constrain the progenitor mass, and then link it with what was obtained in Section 3. For this purpose, we consider three methods: (i) the early bolometric light curve modeling, (ii) the comparison of nebular spectra with synthetic nebular spectra from Dessart et al. (2023a), and (iii) the oxygen mass estimation from the [O I] $\lambda\lambda 6300, 6364$ flux following the procedure of Jerkstrand et al. (2014). Our results are summarized in Fig. 5.

5.1 Hydrodynamical model

We used the 1D Lagrangian hydrodynamic code (Bersten et al. 2011) to model the bolometric light curve and the photospheric velocity

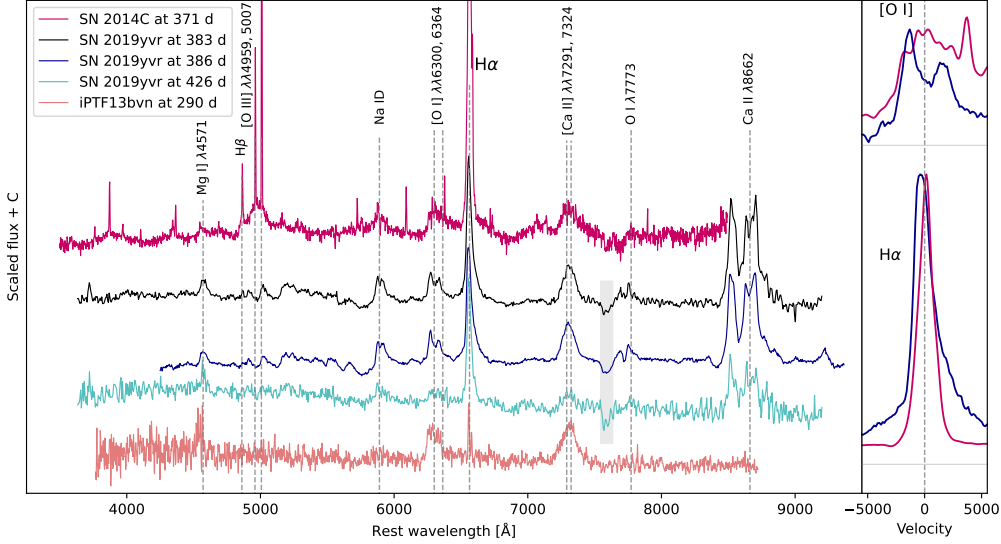


Figure 4. Left panel: nebular spectra of SN 2019yvr compared to the transitional object SN 2014C (Milisavljevic et al. 2015), and to its best match in the early phase, iPTF13bvn (Kuncarayakti et al. 2015). Spectra are corrected by redshift and not corrected by extinction. Prominent emission features are identified and labeled. The telluric A-band in SN 2019yvr is marked with a gray shadow. Right panel: $H\alpha$ and oxygen doublet profiles of SN 2019yvr (+386 d, blue) and SN 2014C (+371 d, pink). The spectrum of SN 2014C has been rebinned in both panels to match the resolution of the SN 2019yvr spectrum. Both interacting events transition to a SN IIn-like spectrum, showing strong $H\alpha$ emission. $H\alpha$ emission lines in iPTF13bvn are not associated with the SN ejecta but with an underlying H II region. Zero velocities are taken at 6300 and 6563 Å.

evolution of SN 2019yvr. As initial configurations for our hydrodynamical models we adopted He stars of different masses from Nomoto & Hashimoto 1988, which follow the complete evolution of the stars with ZAMS masses of 13, 15, 18, and 25 M_{\odot} , to the pre-SN conditions. The simulations’ free parameters are the explosion energy (E), the ejected mass (M_{ej}), the mass of synthesized ^{56}Ni (M_{Ni}), and the extent of outward mixing of ^{56}Ni (as a fraction of the pre-SN mass). The energy is deposited at a certain mass coordinate, M_{cut} , within the pre-SN structure. It is assumed that the matter inside M_{cut} collapses into a compact remnant while the outer mass is ejected.

We computed the bolometric light curve for SN 2019yvr based on ($g - r$) and ($r - i$) color curves using the bolometric-correction versus color calibrations for SNe Ib given by Lyman et al. (2014, see their Table 2). We applied extinction and distance values as given in Section 2 to derive bolometric luminosities, and then averaged the results obtained from both color indices. Finally, to approximate photospheric velocities, we measured the Fe II $\lambda 5169$ line velocity from the location of the absorption minimum.

Figure 5, panels a) and b), show the results of the modeling. Our preferred model corresponds to a pre-SN model with a mass of 3.3 M_{\odot} , $E = 4 \times 10^{50}$ erg, $M_{\text{Ni}} = 0.088 M_{\odot}$ and an extensive mixing of 0.93. We also assume a $M_{\text{cut}} = 1.5 M_{\odot}$, leading to an $M_{ej} = 1.8 M_{\odot}$. However a model with a pre-SN mass of 4 M_{\odot} also produces a reasonable match to the data. Therefore we propose progenitors with a pre-SN mass between 3 and 4 M_{\odot} , which corresponds to a ZAMS mass of 13 – 15 M_{\odot} .

We have also tested models with higher masses which require higher energy in order to reproduce the expansion velocities, leading to worse fitting to the light curve (see Fig. 5, panels a) and b)). For these more massive progenitors, we found that no set of parameters can fit both the bolometric light curve and the velocities together. Specifically, in Figure 5 we show two models corresponding to 8.0 M_{\odot} pre-SN models with $E = 1$ foe and $E = 5$ foe, and equal values for $M_{ej} = 6.2 M_{\odot}$ ($M_{\text{cut}} = 1.8 M_{\odot}$), $M_{\text{Ni}} = 0.1 M_{\odot}$,

and mixing = 0.98. The first case reproduces well the velocities but not the bolometric light curve, and vice versa.

Since the lowest pre-SN mass model provided by Nomoto & Hashimoto (1988) is that of 3.3 M_{\odot} , we are not able to model the bolometric light curve and photospheric velocities for lower masses and constraint the inferior limit of the progenitor star mass with this approach. The derived ZAMS mass between 13 and 15 M_{\odot} thus corresponds to an upper limit.

5.2 Model nebular spectra and the [O I]/[Ca II] ratio

The flux ratio of nebular [O I] $\lambda\lambda 6300, 6364$ to [Ca II] $\lambda\lambda 7291, 7324$ lines has been suggested as an indicator of the pre-SN mass (e.g. Fransson & Chevalier 1989; Maeda et al. 2007; Fang et al. 2022). We calculated these ratios on the +383 and the +426 d EFOSC2 spectra by fitting Gaussian profiles and subtracting the strong local continuum. In the case of [O I], we used two Gaussians to account for the flux, as the line profile is not well fitted by one Gaussian only (see Fig 4, right panel).

We use the grid of models published in Dessart et al. (2023a), where the spectral evolution between 100 and 400 d is calculated for a wide range of initial He masses. We measured the flux ratio [O I]/[Ca II] on these models by fitting a single Gaussian profile centered at 6300 Å for [O I] and at 7304 Å for [Ca II], since the doublets are blended. We compared these results to our measurements in SN 2019yvr at both epochs, as in Figure 5 panel c). This approach yields a progenitor with a helium mass between 3.0 – 3.5 M_{\odot} , which is in agreement with the result from the hydrodynamical model. We note, however, that the line fluxes in the model spectra—which are computed without CSI—are substantially smaller than those obtained for SN 2019yvr. This difference can be due to a contribution from the CSI in the line fluxes. We cannot ascertain how this may affect the flux ratios. Therefore, this caveat should be kept in mind.

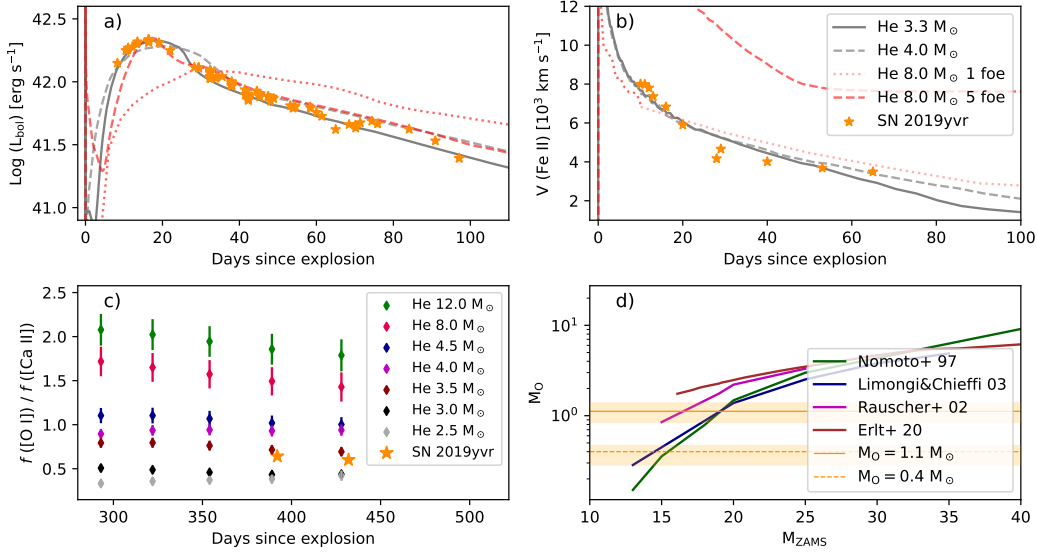


Figure 5. Progenitor mass estimation summary. Panels a) and b) show the bolometric light curve and velocity measurements of SN 2019yvr (orange stars) together with the output of the hydrodynamical models for stars with final He core masses of 3.3, 4.0 and $8.0 M_{\odot}$ (solid, dotted, and dashed lines, respectively; see Section 5.1). The preferred model is the least massive. In panel c) we plot the evolution of oxygen to calcium flux ratio from synthetic spectra (diamonds, Dessart et al. 2023a) and our measurements for SN 2019yvr (orange stars), which fall in the region between 3.0 and $3.5 M_{\odot}$ He core masses (see Section 5.2). Panel d) shows oxygen yields from Nomoto et al. (1997), Limongi & Chieffi (2003) and Rauscher et al. (2002) for different zero-age main sequence masses and the oxygen core mass derived from [O I] doublet flux (see Section 5.3).

5.3 [O I] doublet flux

Following the procedure described in Jerkstrand et al. (2014), we estimate the oxygen core minimum mass responsible for [O I] doublet flux emission. As in Section 5.2, we assume that the flux comes only from the ejecta and has no contribution from the CSI. This is a strong assumption, since it has been shown that at late times the material excited by CSI can play a major role in the spectral features (Dessart et al. 2023b). Furthermore, the models by Dessart et al. 2023a without CSI have much lower lines fluxes, as do the spectra of the SNe that do not appear to have CSI (SN 2011dh and iPFT13bvn). We thus consider this an upper limit for the pre-SN progenitor mass, and leave further analysis on how the CSI may affect the spectral features for the accompanying paper.

The flux measurement is performed as detailed in Section 4 in the dereddened spectrum at +383 d, due to its high quality and minimal host contamination. Temperature estimation from [O I] $\lambda 5777$ is not available due to the absence of the line. We therefore assume a typical temperature for these regions of 3000 K. In these conditions, the estimated core oxygen mass is $\sim 1.1 \pm 0.3 M_{\odot}$. If we assume a higher temperature of 3500 K, the oxygen mass drops to $\sim 0.4 \pm 0.09 M_{\odot}$.

In both cases, following oxygen production yields from Nomoto et al. (1997), Rauscher et al. (2002) and Limongi & Chieffi (2003), the estimates indicate a progenitor mass between 15 and $20 M_{\odot}$ (see Fig. 5, panel d)). This value is somewhat higher than those obtained in Sections 5.1 and 5.2.

6 CONCLUSIONS

We have presented light curves and spectra of SN 2019yvr that show clear signatures of late-time interaction with a CSM. Time-series observations allowed us to constrain the onset of light curve flattening and H α emission line. We estimated the timing of the CSI and thus the CSM distance to the progenitor, as $\sim 6.5 - 9.1 \times 10^{15}$ cm in case it is detached from the SN progenitor star. Assuming a

steady $50 - 100 \text{ km s}^{-1}$ wind velocity, this implies a mass-loss rate of $\sim 3 - 7 \times 10^{-5} M_{\odot} \text{ yr}^{-1}$, occurring up until $\sim 20 - 60$ years prior to the explosion.

Our analysis on the progenitor mass presented in Section 5 is in contradiction with progenitors with pre-SN masses of $\geq 8 M_{\odot}$. Such a star may have started as a single massive star on the ZAMS and lost the outer layers via vigorous winds, but in the case of SN 2019yvr a less massive star that lost its H-rich envelope through binary interactions (e.g., Fang et al. 2019; Drout et al. 2023) is a more plausible scenario. It is also possible that the progenitor star experienced a hybrid mass-loss mechanism as that discussed by Fang et al. (2019) and Sun et al. (2023).

The main question lies in how a progenitor with no hydrogen, as indicated by the early spectra, can lead to a H-rich SN at later times. Kilpatrick et al. (2021) suggested two progenitor scenarios for SN 2019yvr: a massive star that went through a series of eruptions in a luminous blue variable (LBV) phase, or a binary system that led to mass-loss episodes timed years to decades ahead of core collapse. Sun et al. (2022) suggested a hot and compact progenitor in a binary system with a cool and inflated YHG companion. Compared with these works, our results are compatible with the binary progenitor scenario and do not favor a single star going through an LBV phase. By studying the host stellar cluster of SN 2014C, Sun et al. (2020) suggested that the progenitor could have been an $11 M_{\odot}$ star depleted by binary interaction. Otherwise, a single star should have retained its hydrogen-rich envelope to be consistent with the clusters' inferred age. If this is correct, both SNe must have gone through similar evolutionary and mass-loss paths, resulting in stripped progenitors with initial masses well below $20 M_{\odot}$.

DATA AVAILABILITY

Nebular spectra are available in the Wiserep (Yaron & Gal-Yam 2012) database (<https://www.wiserep.org/>).

ACKNOWLEDGEMENTS

The Finnish National Agency for Education (EDUFI) supported this research project through an EDUFI Fellowship. H.K. was funded by the Research Council of Finland projects 324504, 328898, and 353019. M.D.S. is funded by the Independent Research Fund Denmark (IRFD) via Project 2 grant 10.46540/2032-00022B. K.M. acknowledges support from the Japan Society for the Promotion of Science (JSPS) KAKENHI grant (JP20H00174) and by the JSPS Open Partnership Bilateral Joint Research Project between Japan and Finland (JPJSBP120229923). NUTS is funded in part by the Instrument center for Danish Astrophysics (IDA). LCOGT network data were obtained through OPTICON (PI Stritzinger, program ID 2020A/031) and NAO (PI Bose, program ID NAO2020A-017) time allocations. Based on observations made with the Nordic Optical Telescope, owned in collaboration by the University of Turku and Aarhus University, and operated jointly by Aarhus University, the University of Turku and the University of Oslo, representing Denmark, Finland and Norway, the University of Iceland and Stockholm University at the Observatorio del Roque de los Muchachos, La Palma, Spain, of the Instituto de Astrofísica de Canarias. Data were also obtained with ALFOSC, which is provided by the Instituto de Astrofísica de Andalucía (IAA) under a joint agreement with the University of Copenhagen and NOT. This work includes data collected at ESO via program IDs 1103.D-0328, 0105.D-0511 and 1106.D-0811. We thank the Subaru staff for the data taken by the Subaru Telescope (S19B-054); the authors acknowledge the very significant cultural role and reverence that the summit of Maunakea has always had within the indigenous Hawaiian community. We are most fortunate to have the opportunity to conduct observations from this mountain. Y.-Z. Cai is supported by the National Natural Science Foundation of China (NSFC, Grant No. 12303054) and the International Centre of Supernovae, Yunnan Key Laboratory (No. 202302AN360001). A.P. is supported by the PRIN-INAF 2022 project "Shedding light on the nature of gap transients: from the observations to the models". L.G. acknowledges financial support from the Spanish Ministerio de Ciencia e Innovación (MCIN), the Agencia Estatal de Investigación (AEI) 10.13039/501100011033, and the European Social Fund (ESF) "Investing in your future" under the 2019 Ramón y Cajal program RYC2019-027683-I and the PID2020-115253GA-I00 HOSTFLOWS project, from Centro Superior de Investigaciones Científicas (CSIC) under the PIE project 20215AT016, and the program Unidad de Excelencia María de Maeztu CEX2020-001058-M. C.P.G. acknowledges financial support from the Secretary of Universities and Research (Government of Catalonia) and by the Horizon 2020 Research and Innovation Programme of the European Union under the Marie Skłodowska-Curie and the Beatriu de Pinós 2021 BP 00168 programme, from the Spanish Ministerio de Ciencia e Innovación (MCIN) and the Agencia Estatal de Investigación (AEI) 10.13039/501100011033 under the PID2020-115253GA-I00 HOSTFLOWS project, and the program Unidad de Excelencia María de Maeztu CEX2020-001058-M. T.E.M.B. acknowledges financial support from the Spanish Ministerio de Ciencia e Innovación (MCIN), the Agencia Estatal de Investigación (AEI) 10.13039/501100011033, and the European Union Next Generation EU/PRTR funds under the 2021 Juan de la Cierva program FJC2021-047124-I and the PID2020-115253GA-I00 HOSTFLOWS project, from Centro Superior de Investigaciones Científicas (CSIC) under the PIE project 20215AT016, and the program Unidad de Excelencia María de Maeztu CEX2020-001058-M. S.M. acknowledges support from the Research Council of Finland project 350458. M.N. is supported by the European Research Council (ERC) under the European Union's

Horizon 2020 research and innovation programme (grant agreement No. 948381) and by UK Space Agency Grant No. ST/Y000692/1. G.P. acknowledges support from ANID through Millennium Science Initiative Programs ICN12_009.

REFERENCES

- Appenzeller I., et al., 1998, *The Messenger*, **94**, 1
 Bersten M. C., Benvenuto O., Hamuy M., 2011, *ApJ*, **729**, 61
 Buzzoni B., et al., 1984, *The Messenger*, **38**, 9
 Chandra P., Chevalier R. A., Chugai N., Milisavljevic D., Fransson C., 2020, *ApJ*, **902**, 55
 Chevalier R. A., Fransson C., 1994, *ApJ*, **420**, 268
 Chugai N. N., Chevalier R. A., 2006, *ApJ*, **641**, 1051
 Dessart L., Hillier D. J., Sukhbold T., Woosley S. E., Janka H. T., 2021, *A&A*, **656**, A61
 Dessart L., Hillier D. J., Woosley S. E., Kuncarayakti H., 2023a, *arXiv e-prints*, p. [arXiv:2306.12092](https://arxiv.org/abs/2306.12092)
 Dessart L., Gutiérrez C. P., Kuncarayakti H., Fox O. D., Filippenko A. V., 2023b, *A&A*, **675**, A33
 Dimitriadis G., 2019, Transient Name Server Classification Report, **2019-2736**, 1
 Dimitriadis G., Foley R. J., Siebert M. R., Kilpatrick C. D., Corbett H. T., 2019, *The Astronomer's Telegram*, **13375**, 1
 Drout M. R., Göteborg Y., Ludwig B. A., Groh J. H., de Mink S. E., O'Grady A. J. G., Smith N., 2023, *arXiv e-prints*, p. [arXiv:2307.00061](https://arxiv.org/abs/2307.00061)
 Ergon M., et al., 2015, *A&A*, **580**, A142
 Fang Q., Maeda K., Kuncarayakti H., Sun F., Gal-Yam A., 2019, *Nature Astronomy*, **3**, 434
 Fang Q., et al., 2022, *ApJ*, **928**, 151
 Filippenko A. V., Matheson T., Barth A. J., 1994, *AJ*, **108**, 2220
 Fransson C., Chevalier R. A., 1989, *ApJ*, **343**, 323
 Fransson C., et al., 2002, *ApJ*, **572**, 350
 Fremling C., et al., 2016, VizieR Online Data Catalog, [pp J/A+A/593/A68](https://vizier.cesr.fr/vizieR/2016-01-01/J/A+A/593/A68)
 Jerkstrand A., Smartt S. J., Fraser M., Fransson C., Sollerman J., Taddia F., Kotak R., 2014, *MNRAS*, **439**, 3694
 Jerkstrand A., Ergon M., Smartt S. J., Fransson C., Sollerman J., Taubenberger S., Bersten M., Spyromilio J., 2015, *A&A*, **573**, A12
 Kilpatrick C. D., et al., 2021, *MNRAS*, **504**, 2073
 Kuncarayakti H., et al., 2015, *A&A*, **579**, A95
 Kuncarayakti H., et al., 2018, *ApJ*, **854**, L14
 Kuncarayakti H., et al., 2022, *ApJ*, **941**, L32
 Limongi M., Chieffi A., 2003, *ApJ*, **592**, 404
 Liu Y.-Q., Modjaz M., Bianco F. B., Graur O., 2016, *ApJ*, **827**, 90
 Lyman J. D., Bersier D., James P. A., 2014, *MNRAS*, **437**, 3848
 Maeda K., et al., 2007, *ApJ*, **658**, L5
 Maeda K., et al., 2015, *ApJ*, **807**, 35
 Margutti R., et al., 2017, *ApJ*, **835**, 140
 Masci F. J., et al., 2019, *PASP*, **131**, 018003
 Matheson T., Filippenko A. V., Ho L. C., Barth A. J., Leonard D. C., 2000, *AJ*, **120**, 1499
 Mauerhan J. C., Filippenko A. V., Zheng W., Brink T. G., Graham M. L., Shivvers I., Clubb K. I., 2018, *MNRAS*, **478**, 5050
 Milisavljevic D., et al., 2015, *ApJ*, **815**, 120
 Muller T., Antilen J., Wiseman P., Yaron O., 2019, Transient Name Server Classification Report, **2019-2903**, 1
 Noguchi K., et al., 2002, *PASJ*, **54**, 855
 Nomoto K., Hashimoto M., 1988, *Phys. Rep.*, **163**, 13
 Nomoto K., Hashimoto M., Tsujimoto T., Thielemann F. K., Kishimoto N., Kubo Y., Nakasato N., 1997, *Nuclear Phys. A*, **616**, 79
 Patat F., Chugai N., Mazzali P. A., 1995, *A&A*, **299**, 715
 Podsiadlowski P., Langer N., Poelarends A. J. T., Rappaport S., Heger A., Pfahl E., 2004, *ApJ*, **612**, 1044
 Rauscher T., Heger A., Hoffman R. D., Woosley S. E., 2002, *ApJ*, **576**, 323
 Rodríguez Ó., Maoz D., Nakar E., 2022, *arXiv e-prints*, p. [arXiv:2209.05552](https://arxiv.org/abs/2209.05552)
 Schlafly E. F., Finkbeiner D. P., 2011, *ApJ*, **737**, 103

- Schlegel E. M., 1990, *MNRAS*, **244**, 269
- Shappee B. J., et al., 2016, *ApJ*, **826**, 144
- Smartt S. J., et al., 2015, *A&A*, **579**, A40
- Smith N., 2014, *ARA&A*, **52**, 487
- Srivastav S., Anupama G. C., Sahu D. K., 2014, *MNRAS*, **445**, 1932
- Stritzinger M., et al., 2012, *ApJ*, **756**, 173
- Stritzinger M. D., et al., 2018, *A&A*, **609**, A135
- Stritzinger M. D., et al., 2023a, *arXiv e-prints*, p. arXiv:2309.05031
- Stritzinger M. D., et al., 2023b, *A&A*, **675**, A82
- Sun N.-C., Maund J. R., Crowther P. A., 2020, *MNRAS*, **497**, 5118
- Sun N.-C., Maund J. R., Crowther P. A., Hirai R., Kashapov A., Liu J.-F., Liu L.-D., Zapartas E., 2022, *MNRAS*, **510**, 3701
- Sun N.-C., Maund J. R., Crowther P. A., 2023, *MNRAS*, **521**, 2860
- Taddia F., et al., 2013, *A&A*, **555**, A10
- Tartaglia L., et al., 2021, *A&A*, **650**, A174
- Thomas B. P., et al., 2022, *ApJ*, **930**, 57
- Tonry J., et al., 2019, *Transient Name Server Discovery Report*, **2019-2726**, 1
- Vinko J., et al., 2017, *ApJ*, **837**, 62
- Woosley S. E., Langer N., Weaver T. A., 1993, *ApJ*, **411**, 823
- Yaron O., Gal-Yam A., 2012, *PASP*, **124**, 668
- Yoon S.-C., 2017, *MNRAS*, **470**, 3970

The metamorphosis of the Type Ib SN 2019yvr: late-time interaction

Supplementary Material

29 January 2024

1 DISCOVERY, ESTIMATED EXPLOSION TIME AND DISTANCE

The discovery of SN 2019yvr was reported to the Transient Name Server (TNS) by the Asteroid Terrestrial-impact Last Alert System (ATLAS) based on images obtained on 2019 December 27.5 UT (i.e., JD=2458845.02) with an apparent *o*-band AB magnitude of 15.9 (?). Two days after the discovery report, this transient was classified as a SN Ib (??). With J2000 coordinates of R.A. = $12^h 45^m 08^s .135$ and Decl. = $-00^\circ 27' 32'' .83$, SN 2019yvr is located within the nearby spiral galaxy NGC 4666.

According to the discovery report, the last ATLAS non-detection occurred on 2019 December 11.6 UT (?), while more constraining non-detection limits come from the Zwicky Transient Facility (ZTF, ?) public data stream. According to ALERCE (?), the best previous ZTF non-detection limit corresponds to a *g*-band magnitude of 19.36 based on an image obtained on 2019 December 18.6 UT (i.e., JD = 2458836.05). ? also reported to TNS a recovered detection of SN 2019yvr with a magnitude of 15.8 based on an open filter image taken on 2019 December 26.2 (i.e., JD = 2458843.73). Taking the mid-point between the last ZTF non-detection and the recovered detection, we adopt the explosion epoch as JD = 2458839.89 ± 3.84 .

NED reports a heliocentric redshift for the host galaxy NGC 4666 of $z = 0.005047$, along with a handful of Tully-Fisher based distances. Fortunately, NGC 4666 also hosted the Type Ia SN ASASSN-14lp that suggests a distance of 14.7 ± 1.5 Mpc, or $\mu = 30.8 \pm 0.2$ mag (?). This value is adopted to set the absolute flux scale of SN 2019yvr.

2 PHOTOMETRIC AND SPECTROSCOPIC DATA

Table 1 provides the details of the photometric observations of SN 2019yvr in the *BVgr*i bands. Table 2 gives the specifications of the spectroscopic observations included in this work.

3 REDDENING ESTIMATION

Details on the reddening estimation methods are presented below. We have considered the typical value of $R_V = 3.1$. ? derive an R_V of $4.7^{+1.3}_{-3}$, but we consider it to be unconstrained. This is most probably due to the lack of near-infrared colors (see ?). Our assumption is well within 1σ of the value derived by ?.

3.1 Color curves

We estimated the host-galaxy reddening from color curves for (*B*−*V*), (*g*−*r*), (*r*−*i*) and (*B*−*i*) comparing them with templates from ? (see Figure 3.1). We calculated the color excess for each point of the color curve and then computed an average color excess for

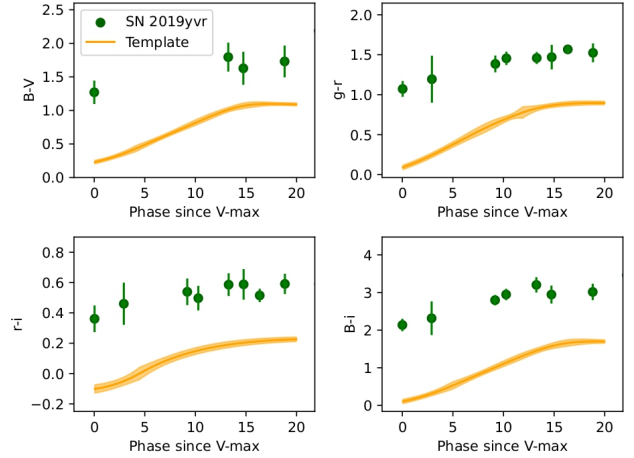


Figure 1. Apparent (*B*−*V*), (*g*−*r*), (*r*−*i*), and (*B*−*i*) color-curves of SN 2019yvr (green dots) extending between +0 d to +20 d, compared with the intrinsic color-curve templates from ? (orange lines).

each one of the four color indices. Finally, we transformed them to $E(B - V)$ assuming an extinction law of ? with $R_V = 3.1$ (? , Table 6) and took a weighted average. The host-galaxy reddening results $E(B - V)_{\text{host}} = 0.57 \pm 0.09$ mag.

3.2 DIB and Na I D absorption

The equivalent width (EW) of absorption features of the diffuse interstellar band (DIB) at 5780 \AA and Na I D have been used for reddening estimation (?). These features are present in our high-resolution spectrum from the Subaru telescope (see Figure 3.2). The DIB absorption feature is found to have an EW $\sim 0.26 \text{ \AA}$, which leads to a reddening of $E(B - V)_{\text{host}} = 0.4$ mag through the method of ?, with an uncertainty of $\sim 50\%$. In the case of Na I D, its EW is $\sim 2.1 \text{ \AA}$, falling at the higher end of the relation proposed by ? and thus not considered reliable for reddening estimation. Its profile with absorptions at four different velocities is an indicator that multiple clouds are located between the SN and the observer.

We find the method based on the color curves (see Section 3.1) to be more reliable, and consistent with values derived from the DIB absorption, and therefore we adopt the $E(B - V)_{\text{host}}$ value obtained in Section 3.1 for our analysis.

4 SN 2019YVR SPECTRAL SERIES

In Section 3.1, four spectra are presented showing the regions of interest for our analysis, showing the He I $\lambda 6678$ and He I $\lambda 7065$

Table 1. Photometric observations of SN 2019yvr.

JD	Telescope+instrument	<i>B</i>	<i>V</i>	<i>g</i>	<i>r</i>	<i>i</i>
2458847.7	NOT+ALFOSC	17.21 ± 0.04	16.10 ± 0.09	...	15.70 ± 0.06	15.42 ± 0.15
2458848.8	1m0-09+fa04	17.00 ± 0.08	...	16.45 ± 0.08	15.58 ± 0.08	15.36 ± 0.08
2458851.6	1m0-12+fa06	16.69 ± 0.07	...	16.16 ± 0.04	15.31 ± 0.05	15.05 ± 0.04
2458852.7	NOT+ALFOSC	16.80 ± 0.07	15.77 ± 0.05	...	15.27 ± 0.03	15.03 ± 0.05
2458853.8	1m0-09+fa04	16.71 ± 0.08	...	16.10 ± 0.08	15.19 ± 0.07	14.90 ± 0.07
2458856.9	1m0-06+fa07	16.70 ± 0.09	...	16.10 ± 0.08	15.08 ± 0.03	14.75 ± 0.04
2458856.9	1m0-08+fa05	16.73 ± 0.30	15.16 ± 0.07	14.83 ± 0.07
2458859.6	1m0-10+fa16	16.93 ± 0.15	15.63 ± 0.08	...	15.11 ± 0.06	14.74 ± 0.06
2458862.5	1m0-10+fa16	17.19 ± 0.44	...	16.52 ± 0.27	15.30 ± 0.11	14.83 ± 0.09
2458868.8	1m0-09+fa04	17.96 ± 0.12	15.67 ± 0.06	15.12 ± 0.06
2458869.9	1m0-06+fa07	18.12 ± 0.20	...	17.16 ± 0.08	15.66 ± 0.05	15.15 ± 0.06
2458869.9	1m0-08+fa05	18.17 ± 0.19	...	17.09 ± 0.14
2458872.9	1m0-04+fa03	18.29 ± 0.29	16.62 ± 0.08	...	15.94 ± 0.05	15.16 ± 0.05
2458872.9	1m0-08+fa05	18.57 ± 0.28	...	17.24 ± 0.10	15.77 ± 0.07	15.25 ± 0.07
2458874.4	1m0-12+fa06	17.76 ± 1.43	...	17.41 ± 0.14	15.92 ± 0.07	15.31 ± 0.08
2458878.4	1m0-10+fa16	18.55 ± 0.26	...	17.59 ± 0.11	16.01 ± 0.06	15.41 ± 0.08
2458878.5	1m0-13+fa14	18.41 ± 0.35	16.75 ± 0.11	...	16.08 ± 0.06	15.47 ± 0.07
2458881.9	1m0-06+fa07	19.05 ± 0.51	16.84 ± 0.15	...	16.15 ± 0.07	15.54 ± 0.07
2458882.8	1m0-05+fa15	18.76 ± 0.13	...	17.78 ± 0.08	16.29 ± 0.05	15.59 ± 0.04
2458882.8	1m0-09+fa04	18.81 ± 0.13	...	17.76 ± 0.09	16.34 ± 0.08	15.74 ± 0.10
2458885.7	1m0-04+fa03	18.58 ± 0.32	...	17.71 ± 0.19	16.29 ± 0.05	15.66 ± 0.04
2458888.6	1m0-12+fa06	18.72 ± 0.47	16.96 ± 0.11	...	16.36 ± 0.07	15.77 ± 0.06
2458889.4	1m0-13+fa14	18.93 ± 1.01	...	17.83 ± 0.42	16.38 ± 0.13	15.63 ± 0.09
2458894.4	1m0-12+fa06	18.76 ± 0.34	...	17.90 ± 0.22	16.50 ± 0.07	15.89 ± 0.06
2458893.7	NOT+ALFOSC	18.96 ± 0.09	17.29 ± 0.07	...	16.51 ± 0.06	...
2458900.5	1m0-13+fa14	18.84 ± 0.20	...	18.07 ± 0.13	16.57 ± 0.06	16.03 ± 0.06
2458905.5	1m0-12+fa06	19.24 ± 0.16	...	18.28 ± 0.08	16.95 ± 0.06	16.27 ± 0.07
2458909.0	1m0-11+fa12	19.11 ± 0.32	...	18.21 ± 0.18	16.82 ± 0.06	16.23 ± 0.06
2458910.7	1m0-09+fa04	19.08 ± 0.16	17.69 ± 0.10	18.21 ± 0.10	16.85 ± 0.09	16.33 ± 0.11
2458910.6	NOT+ALFOSC	19.17 ± 0.15	17.65 ± 0.11	18.24 ± 0.09	16.88 ± 0.11	16.17 ± 0.07
2458916.4	1m0-13+fa14	19.03 ± 0.89	...	18.31 ± 0.56	16.83 ± 0.18	16.20 ± 0.11
2458924.6	1m0-05+fa15	19.01 ± 0.18	...	18.29 ± 0.09	16.92 ± 0.07	16.31 ± 0.07
2458931.4	1m0-13+fa14	19.23 ± 0.25	...	18.41 ± 0.16	17.12 ± 0.07	16.58 ± 0.07
2458937.6	NOT+ALFOSC	19.69 ± 0.13	17.95 ± 0.07	18.73 ± 0.07	17.60 ± 0.04	...
2458956.5	NOT+ALFOSC	19.79 ± 0.10	18.45 ± 0.08	18.75 ± 0.09	17.35 ± 0.04	17.08 ± 0.08
2458964.2	1m0-03+fa19	19.31 ± 0.31	17.90 ± 0.15	18.58 ± 0.23	17.29 ± 0.11	16.79 ± 0.09
2458968.6	NOT+ALFOSC	19.69 ± 0.31	18.12 ± 0.12	18.60 ± 0.10	17.36 ± 0.19	16.78 ± 0.10
2458985.5	NOT+ALFOSC	19.88 ± 0.16	18.56 ± 0.07	18.81 ± 0.07	17.46 ± 0.05	16.97 ± 0.06
2459011.4	NOT+ALFOSC	19.76 ± 0.32	18.28 ± 0.13	18.84 ± 0.10	17.57 ± 0.05	17.11 ± 0.06
2459033.4	NOT+ALFOSC	...	18.45 ± 0.16	19.02 ± 0.14	17.65 ± 0.06	17.15 ± 0.10
2459038.4	NOT+ALFOSC	...	18.61 ± 0.09	19.01 ± 0.07	17.82 ± 0.03	17.35 ± 0.06
2459201.7	NOT+ALFOSC	...	19.97 ± 0.25	19.81 ± 0.18	18.88 ± 0.16	18.16 ± 0.43

Table 2. Journal of spectroscopic observations of SN 2019yvr. The uncertainties were computed by adding in quadrature the photometry error and the nightly zero-point error.

JD	Phase [d] ^a	Telescope+instrument	t _{exp} [s]
2458853.0	+1	Subaru+HDS	5400
2458853.8	+2	NTT+EFOSC2	180
2458893.6	+42	NOT+ALFOSC	3600
2458910.6	+59	NOT+ALFOSC	3600
2458930.7	+79	NTT+EFOSC2	1500
2458969.4	+118	NOT+ALFOSC	2400
2459234.7	+383	NTT+EFOSC2	3200
2459237.8	+386	VLT+FORIS2	2740
2459277.8	+426	NTT+EFOSC2	3100

^aPhase is relative to the epoch of *B*-band maximum, i. e., JD = 2458851.6.

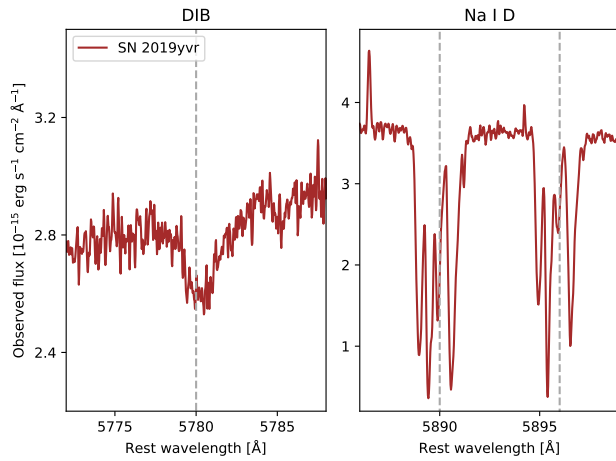


Figure 2. Subaru+HDS spectrum of SN 2019yvr obtained on +2 d (i. e., 2020 January 4.6 UT). Left panel: the diffuse interstellar band (DIB) at 5780 Å. Right panel: the Na I D interstellar lines. Gray dashed lines indicate the rest wavelength for all features.

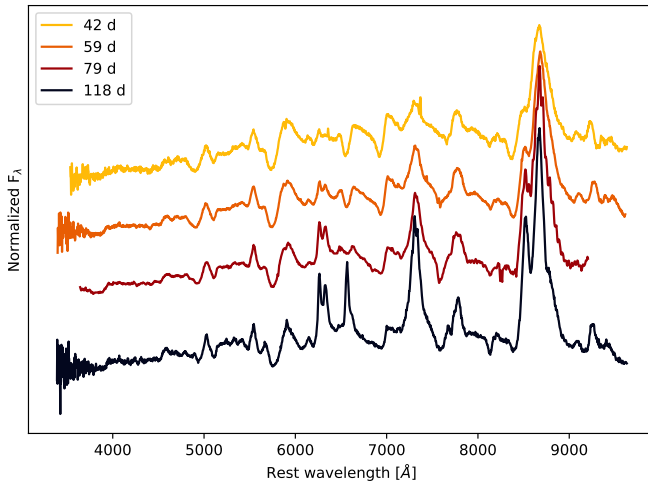


Figure 3. Optical low-resolution spectra of SN 2019yvr spanning +42 d and +118 d.

lines. In Figure 3 these spectra are displayed entirely. The evolution spans from +42 to +118 d post-maximum and depicts the rise of the H α emission line. Observations details can be found in Table 2.